

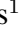
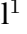









Observation and origin of non-thermal hard X-rays from Jupiter

Kaya Mori¹ , Charles Hailey¹ , Gabriel Bridges¹ , Shifra Mandel¹ , Amani Garvin¹, Brian Grefenstette² , William Dunn^{3,4,5} , Benjamin J. Hord^{6,7} , Graziella Branduardi-Raymont^{3,4} , John Clarke⁸, Caitriona Jackman⁹ , Melania Nynka⁸  and Licia Ray¹⁰ 

¹*Columbia Astrophysics Laboratory, Columbia University, New York, NY 10027, USA*

²*Cahill Center for Astronomy and Astrophysics, California Institute of Technology, Pasadena, CA 91125, USA*

³*Mullard Space Science Laboratory, Department of Space and Climate Physics, University College London, Dorking, UK*

⁴*The Centre for Planetary Science at UCL/Birkbeck, London, UK*

⁵*Harvard-Smithsonian Center for Astrophysics, Smithsonian Astrophysical Observatory, Cambridge, MA 02138, USA*

⁶*Department of Astronomy, University of Maryland, College Park, MD 20742-2421, USA*

⁷*NASA Goddard Space Flight Center, Greenbelt, MD 20771, USA*

⁸*Kavli Institute For Astrophysics and Space Research, Massachusetts Institute of Technology, Cambridge, MA 02139, USA*

⁹*Astronomy and Astrophysics Section, Dublin Institute for Advanced Studies, Dublin, Ireland*

¹⁰*Department of Physics, Lancaster University, Lancaster, UK*

Electrons accelerated on Earth by a rich variety of wave scattering or stochastic processes^{1,2}

generate hard non-thermal X-ray bremsstrahlung up to $\gtrsim 1 \text{ MeV}^{3,4}$ and power Earth's various types of aurorae. Although Jupiter's magnetic field is an order of magnitude larger than Earth's, space-based telescopes have previously detected X-rays only up to $\sim 7 \text{ keV}^5$. Based on theoretical models of the Jovian auroral X-ray production^{6–8}, X-ray emission in the $\sim 2\text{--}7 \text{ keV}$ band has been interpreted as thermal (arising from electrons characterized by a Maxwell-Boltzmann distribution) bremsstrahlung^{5,9}. Here we report the observation of hard X-rays in the 8–20 keV band from the Jovian aurorae, obtained with the *NuSTAR* X-ray observatory. The X-rays fit to a flat power-law model with slope 0.60 ± 0.22 – a spectral signature of non-thermal, hard X-ray bremsstrahlung. We determine the electron flux and spectral shape in the keV–MeV energy range using coeval in-situ measurements by the Juno spacecraft's JADE and JEDI instruments. Jovian electron spectra of the form we observe have previously been interpreted to arise in stochastic acceleration, rather than coherent acceleration by electric fields¹⁰. We reproduce the X-ray spectral shape and approximate flux observed by *NuSTAR*, as well as explain the non-detection of hard X-rays by *Ulysses*¹¹, by simulating the non-thermal population of electrons undergoing precipitating electron energy loss, secondary electron generation and bremsstrahlung emission in a model Jovian atmosphere. The results highlight the similarities between the processes generating hard X-ray auroras on Earth and Jupiter, which may be occurring on Saturn, too.

NuSTAR, launched in 2012, is the first space-based focusing hard X-ray telescope¹². Given its broad energy band (3–79 keV) and sub-arcminute angular resolution, *NuSTAR* provides sufficient sensitivity to detect hard X-ray emission from Jupiter and spatially resolve the northern and

southern aurorae. From 2015 to 2018, we conducted five *NuSTAR* observations of Jupiter (with a total exposure time of 600 ksec), four of which coincided with Perijoves (PJ) 6, 7 and 12 and Apojove (AJ) 7 of *Juno*'s orbits (Extended Data Table 1). The *NuSTAR* observations during PJ 7 and AJ 7 overlapped with *XMM-Newton* observations, which are included in the subsequent analysis. In each of the observations, *NuSTAR* detected X-ray emission from Jupiter with net count rates of $\sim 1.2 \times 10^{-3}$ cts s $^{-1}$ on average, and significance ranging between $(3 - 5)\sigma$ in the 3–20 keV band. We found no significant detection ($\lesssim 1\sigma$) above 20 keV. Detection significance is defined as $S = \frac{N_T - N_B}{\sqrt{N_T + N_B}}$, where N_T and N_B are total (source+background) and background counts, extracted from a circle with $r = 45''$ (which contains the entire planet) and an annulus at $r = 60\text{--}75''$, respectively. Since we did not detect significant flux variability among the *NuSTAR* observations (Methods), we combined imaging and spectral data from all *NuSTAR* observations, allowing us to explore the persistent hard X-ray emission above 8 keV with improved photon statistics. Unlike the recent timing studies with *XMM-Newton* and *Chandra*^{13,14}, any variable components related to the solar wind are likely to be time averaged in our *NuSTAR* analysis. A recent *XMM-Newton* observation revealed that the persistent auroral X-ray emission is largely due to charged particles accelerated inward from the Io plasma disk⁹, which is the Jovian reservoir of electrons and ions emitted from the volcanically active moon Io¹⁵.

We detected hard X-ray emission from Jupiter in the 8–20 keV band with 7σ significance in the combined images. Figure 1 shows a *NuSTAR* 8–20 keV image of Jupiter in the planet's co-moving frame, clearly resolving hard X-ray emission from the two auroral regions. Above ~ 20 keV, we found no significant detection exceeding $\sim 2\sigma$. The *NuSTAR* observations show

higher fluxes from the southern aurora, by a factor of 2.1 ± 0.1 and 2.0 ± 0.2 in the 3–20 and 8–20 keV bands, respectively. The observed divergence in brightness is intrinsic and not due to the visibility of the auroral regions, which suggest $\sim 7\%$ higher visibility for the northern aurora (Methods). The brighter southern aurora above 3 keV is in stark contrast to the softer X-ray band, where ion line emission is predominant and the northern aurora is consistently brighter¹⁶. We also confirmed that the northern aurora is brighter than its southern counterpart by a factor of 2.9 ± 0.1 in the $E = 0.3\text{--}3$ keV EPIC images of the *XMM-Newton* observations, which are simultaneous with two of the *NuSTAR* observations (AJ7 and PJ7). This contrast between the aurorae is further emphasized by the often incoherent X-ray pulsation signals¹⁶. Together, these observations suggest that the X-ray emission of the southern aurora may be more controlled by the energetic flow of electrons, and the northern aurora by precipitation of sulfur and oxygen ions and charge exchange processes, since the southern pole exhibits more persistent and higher electron currents, as revealed by recent *Juno/MAG* observations¹⁷.

We found no significant difference in the spectral hardness ratio between the northern and southern aurorae (Methods). This allowed us to perform joint spectral analysis for the two emission regions, improving fit statistics. We extracted *NuSTAR* and *XMM-Newton*-EPIC spectra from a $r = 45''$ circle around the Jovian center. *NuSTAR* and *XMM-Newton*-EPIC background spectra were taken from an annular region at $r = 60\text{--}75''$ and a nearby source-free rectangular region, respectively. Joint *NuSTAR* and *XMM-Newton* spectra are shown in Figure 2. The *NuSTAR* and *XMM-Newton* spectra are fit to a power-law model with the best-fit photon index $\Gamma = 0.60 \pm 0.22$ ($\chi^2_\nu = 1.09$ for 34 dof). In contrast, high temperature thermal bremsstrahlung ($kT \sim 30\text{--}200$ keV),

previously suggested by *XMM-Newton* observations⁹, has a markedly different shape and yields a poor fit in the 3–20 keV band ($\chi^2_\nu = 1.5$ for 34 dof). Our simulation of a thermal bremsstrahlung model, using telescope response files, resulted in a much softer X-ray spectrum with $\Gamma > 1.3$. The observed hard spectral index is a signature of non-thermal bremsstrahlung emission and is only discernible from thermal emission through fitting the broadband *NuSTAR* data.

Exploiting simultaneous *Juno* and *NuSTAR* data presents a unique opportunity to use observed, non-thermal electron fluxes and spectra, and an appropriate model, to ab initio predict the hard X-ray flux and spectrum for direct comparison with the X-ray observations. Consequently we simulated X-ray bremsstrahlung spectra from precipitating electrons measured by *Juno*'s JADE and JEDI instruments. We extracted JADE and JEDI electron spectra from PJ 6,7 and 12, ranging in energy from 0.1 keV to 1 MeV¹⁸. The downward electron current into the atmosphere was selected by confining the range of pitch angles at $\theta \leq 44^\circ$ (northern aurora) and $\theta \leq 37^\circ$ (southern aurora)¹⁹ with respect to the magnetic field orientation measured by the *Juno*/MAG instrument²⁰. Broadband JADE/JEDI electron spectra from $E_e \sim 1$ keV to ~ 1 MeV are well characterized by a power-law model ($N(E_e) \sim E_e^{-\alpha_e}$) with $\alpha_e = 0.7$ – 1.9 (Figure 3). We interpret these near-smooth spectra, with no evidence of a peak in phase space, as indicative of a stochastic, or broadband, as opposed to coherent acceleration process, as has been argued for spectra from previous *Juno* observations²¹. We found that the electron spectral shape, solely extracted from the *Juno* data, is insensitive to the selection of a loss cone range. We then simulated X-ray bremsstrahlung spectra using the GEANT4 particle propagation simulator²². In each simulation, we injected a beam of 100 million electrons – which were generated randomly from a power-law model with mean spectral

index $\alpha_e = 1.3$, calculated from the observed JADE/JEDI electron spectra (Figure 3) – into a stratified spherical shell that mimics the Jovian atmosphere (Methods). The most accurately determined chemical composition and density/temperature profile of the atmosphere in the polar regions have been implemented in our simulation^{23,24}. All primary electrons, electrons generated by collisional ionization and X-ray bremsstrahlung photons are tracked. We recorded X-ray photons that escape the model atmosphere to construct bremsstrahlung X-ray spectra.

Inserting the full JADE and JEDI electron spectrum into the GEANT4 simulation that realistically models the Jovian atmosphere yielded a spectrum that reproduces the features observed in the broadband *NuSTAR* and *XMM-Newton* X-ray data. These include both the observed X-ray power law with an effective photon index of $\Gamma \approx 0.6$ (3–20 keV) and a gradual spectral softening at $\gtrsim 20$ keV. The observed and simulated spectral softening explain the *Ulysses* non-detection of X-rays above 27 keV. This consistency confirms that the observed hard X-rays are indeed generated by these electrons. One of the earlier *XMM-Newton* observations, fitting the narrow 2–7 keV energy band, also detected a flat power-law component and an extrapolated flux at 27–48 keV that was inconsistent with the *Ulysses* non-detection, indicating a rollover below 50 keV.⁵ These key features are robust; they are apparent over the entire range of electron spectral indices ($\alpha_e = 0.7$ –1.9) measured by *Juno* (Figure 4). The predicted X-ray flux, calculated by combining all the downward electron data from the PJ6, 7 and 12 orbits, is lower than the observed flux by a factor of 1.4–4, depending on the electron spectrum selection (Methods). This is excellent agreement, considering the sensitivity of the result to the spatial and temporal variability of the electron flux, statistical uncertainties associated with the selection of the electron loss cone, the precise size of

the X-ray emitting area, and the neglect of magnetic mirroring. Our simulations indicate that the bulk of the bremsstrahlung X-rays originate at an altitude ~ 200 km (corresponding to a neutral hydrogen column density $N_{\text{H}} \sim 10^{22} \text{ cm}^{-2}$) above Jupiter’s surface (defined as a pressure of 1 bar). This is substantially deeper in the stratosphere compared to findings from previous work, which assumed that the X-rays were generated by thermal bremsstrahlung, resulting in peak emission at altitudes of $\sim 260\text{--}340$ km⁸. The comparable upwelling flux of electrons observed by *Juno* was ignored in our simulations. Those electrons must originate at much higher altitudes, where X-ray emission is negligible due to the low atmospheric density. Otherwise, the upwelling electron spectrum would have been substantially different than what *Juno* observed, due to electron energy losses in the denser stratosphere.

Our interpretation of Jovian X-ray spectra has relied on forward folding a detailed model of the Jovian atmosphere with the relevant X-ray emission physics, using coeval *Juno* electron data as initial input, as has been done for similar Earth X-ray auroral analysis²⁵. But the X-ray spectra alone encode substantial information about the most energetic electrons. Greater than 95% of the *NuSTAR* band X-rays arise from $\gtrsim 100$ keV electrons, and the bulk of the X-rays arise from $\sim 700 - 1000$ keV electrons. Thus unfolding Jovian hard X-ray spectra can provide the novel capability of extracting correlated electron spectra when such information is not otherwise available. This high energy electron probe is possible because the electron-energy dependence of the X-ray bremsstrahlung cross-section and the higher molecular densities required for X-ray emission both favor more energetic electrons. While electron spectra from coherent B-field aligned acceleration differ from those produced by stochastic acceleration, similar considerations suggest

that unfolding hard X-ray spectra is unlikely to permit discrimination between the acceleration processes; the X-ray observation times would have to be much longer, as the periods of such coherent electron acceleration are rarer than the stochastic processes¹⁰.

Broadband *NuSTAR* X-ray observations have provided clear evidence of non-thermal, hard X-ray bremsstrahlung from a Solar System body other than Earth. The observed spectral shape and flux arise naturally from non-thermal electron precipitation, energy loss and subsequent X-ray emission in the Jovian atmosphere. The coeval JADE/JEDI electron spectra associated with our X-ray spectra show the unambiguous signatures of stochastic or broadband acceleration of non-thermal electrons, in analogy to the interpretation established in previous work by the JEDI/JADE teams¹⁰, and similar to processes responsible for the diffuse aurorae on Earth¹⁻⁴. No longer are unphysically high electron temperatures of $kT \gtrsim 100$ keV⁹, such as are typically seen in stellar objects, required to fit the harder part of the X-ray spectrum. And the non-thermal X-ray bremsstrahlung spectrum naturally softens above 20 keV, explaining the *Ulysses* non-detection in the 28–45 keV band¹¹. Further hard X-ray bremsstrahlung studies of Jupiter will provide a fruitful approach to elucidating Jovian magnetospheric physics, as such studies have on Earth. Moreover, an intense, bi-directional, non-thermal electron spectrum has also been observed from the magnetosphere of Saturn²⁶, and holds out the prospect that deep, hard X-ray observations may yet reveal a third planet with non-thermal hard X-ray bremsstrahlung.

Methods

X-ray observations and data reduction. *NuSTAR* observed Jupiter five times from 2015 to 2018 with a total exposure of ~ 600 ksec. Besides the first observation in 2015, the *NuSTAR* observations coincided with Juno’s perijoves (PJ 6, 7 and 12) or apojove (AJ 7) as shown in Extended Data Table 1. In each *NuSTAR* observation, a series of multiple *NuSTAR* pointings were consecutively performed by tracking the (moving) target close to the on-axis position. Using JPL’s HORIZONS ephemeris data, we corrected all photon event positions to Jupiter’s comoving frame. The absolute astrometric accuracy of *NuSTAR* is $\pm 5''$ (90%)¹² which was confirmed by comparing the optical and *NuSTAR* positions of a background AGN (SDSS J092412.11+161135.5)²⁸ in the 2015 observation. For the other *NuSTAR* observations in 2017–2018, no X-ray sources were observed in the field of view. All *NuSTAR* data were processed using the `nupipeline` command¹². We processed EPIC data from the two *XMM-Newton* observations coinciding with the *NuSTAR* observations in June 18 and July 10, 2017 using SAS version 16.1.0. Similar to the *NuSTAR* data, we modified all photon event positions to Jupiter’s comoving frame.

Visibility of the Jovian aurorae regions. To compute the visibility of the northern and southern aurora, the left handed Sys III latitudes and longitudes for the main auroral ovals were obtained from the LASP Magnetospheres of Outer Planets Group (<https://lasp.colorado.edu/home/mop/missions/juno/trajectory-information>). The Jupiter ephemeris was gathered from JPL’s HORIZONS database. The auroral ovals were orthographically projected and the total visible projected area was computed for every interval within a *NuSTAR* observation. The areas of the northern and southern aurorae were compared in this way and we found that the

northern aurora was on average 7.2% more visible than the southern aurora during the *NuSTAR* observations.

Background analysis. *NuSTAR* background below ~ 30 keV is dominated by stray-light photons – X-ray photons from point sources and diffuse X-ray emission outside the field of view and therefore not reflected by the optics. The Galactic latitude of Jupiter’s position during the *NuSTAR* observations ranged from 32° to 59° . Stray-light background from the Galactic Ridge X-ray emission did not significantly affect our analysis; this was confirmed by the lack of Fe emission lines in the background spectra. Based on the `nuskybkg` tool²⁹, we found that the *NuSTAR* background, mostly due to the stray-light background from cosmic X-ray diffuse emission, is not spatially uniform on the detector plane. Therefore, we extracted *NuSTAR* background counts and spectra, from an annulus close to the source, at $r = 60\text{--}75''$ around the Jupiter position. *XMM-Newton* background spectra were extracted from a rectangular region near the source by avoiding the detector chip gaps.

Variability analysis. We studied long-term X-ray variation using *NuSTAR* count rates between the different *NuSTAR* observations. To minimize statistical errors, we generated lightcurves for each observation after combining the FPMA and FPMB data, using a circular extraction region of $r = 45''$. Extended Data Table 1 shows the source counts and detection significance for each *NuSTAR* observation. The detection significance is defined as $S = \frac{N_T - N_B}{\sqrt{N_T + N_B}}$, where N_T and N_B are total (source+background) and background counts, respectively. We did not find any significant variation in the 3–20 keV lightcurves between the *NuSTAR* observations. There has been no prominent solar activity during the *NuSTAR* observations. Our search for short-term (hours)

variability signals using the Bayesian Block algorithm³⁰ yielded no detection, possibly due to the limited statistics. Due to the lack of variability, we stacked *NuSTAR* images and spectra in the subsequent analysis.

Spectral analysis. We extracted *NuSTAR* source spectra and generated detector response files as well as effective area files using the `nuproduct` command¹². We performed spatially-resolved spectral analysis using hardness ratios and stacked *NuSTAR* spectra from each auroral region (defined as a $r = 25''$ circle around the centroid of X-ray spot at each pole). We obtained 114 and 229 net counts (8–20 keV band) from the northern and southern regions, respectively, by combining all the *NuSTAR* observations. We defined the hardness ratios as $HR = (H - S)/(H + S)$, where H and S are the net counts in 3–8 keV and 8–20 keV, respectively. The hardness ratios between the two aurorae, $HR = 0.15 \pm 0.24$ (north) and 0.10 ± 0.11 (south), do not differ statistically significantly. In order to improve the statistics, we stacked 3–30 keV *NuSTAR* spectra extracted from a $r = 45''$ circle around the Jovian center (including both aurorae) and from all the observations listed in Extended Data Table 1. Background spectra were extracted from an annular region at $r = 60\text{--}75''$ around the Jovian center. *NuSTAR* spectra were adaptively rebinned so that each energy bin contains enough source counts to ensure more than 2σ significance over the background counts. For fitting *NuSTAR* spectra, we adopted the 3–22 keV band above which the background dominates. *XMM-Newton*-EPIC source photons were extracted from a circle of $r = 45''$ around the Jovian center, and background photons from a nearby, source-free rectangular region. We adopted the lower energy bound for *XMM-Newton*-EPIC data to be 3 keV in order to ensure that there is no contamination from the CX line emission $\lesssim 2$ keV. Jointly fitting 3–10 keV *XMM-Newton*-EPIC

and 3–30 keV *NuSTAR* spectra with a power-law model, using the detector response and telescope effective area files in XSPEC, yielded a photon index ($\Gamma = 0.60 \pm 0.22$) with $\chi^2_\nu = 1.02$ for 34 dof. Fitting a thermal bremsstrahlung model resulted in the maximum temperature of $kT = 200$ keV allowed in the XSPEC model; the temperature is poorly constrained and the fit yields an unacceptably large reduced chi-squared value of $\chi^2_\nu = 1.51$ for 34 dof. In Figure 2, we present the unfolded *NuSTAR* and *XMM-Newton*-EPIC flux spectra as well as the Ulysses flux upper limit in the 3–50 keV band.

***Juno* JADE and JEDI data analysis.** We extracted in-situ electron data from *Juno* collected during the three perijoves (PJ6, PJ7, and PJ12) coinciding with the *NuSTAR* observations. The JADE³¹ and JEDI³² instruments aboard *Juno* measure the energies and pitch angles of ions and electrons in the 0.1–100 keV and 30–1000 keV band, respectively. The *JADE* and *JEDI* level 3 files were gathered from the Planetary Plasma Interactions node of the NASA Planetary Data System as well as the magnetometer data from the MAG instrument (in payload coordinates)^{33–35}. Additionally, SPICE kernels were acquired from the NAIF data node of the PDS³⁶. JEDI-E level 3 files contain differential intensity and pitch angle data of electrons, while JADE-E level 3 files provide count rates, energies, and look directions of electrons in despun spacecraft coordinates. We converted the JADE-E electron data to differential intensity distribution [electrons/cm²/s/keV/sr], following the methodology of Allegrini³⁷. A conversion from despun spacecraft coordinates to pitch angles was performed using the transformation matrix data provided in the level 3 files and the SPICE kernel data as well as the MAG magnetic field data. We converted the channel number to kinetic energy [keV] for each JEDI electron event using the calibration files. For each of the

three perijoves (PJ 6, 7 and 12), we selected two time intervals corresponding to *Juno*'s passages over the northern and southern poles (Extended Data Table 2). For each of the six time intervals, electron event times were selected when *Juno*'s magnetic footprint was close to the auroral ovals³⁸ ($1.5 - 2.6R_J$ or 42,500 - 117,500 km above the surface) and JADE-E recorded high net count rates ($\sim 10^8$ cts s^{-1} above the background level).

Only precipitating electrons are considered in this investigation. As shown later (cf. figure 5), the X-ray emission peaks deep in the stratosphere, where the equivalent hydrogen column density is $N_H \sim 10^{22}$ cm^{-2} . Simulations using GEANT demonstrate that the upwelling electron spectrum would be substantially modified by ionization energy losses from that observed by *Juno* unless electrons originate at much higher altitudes than the stratosphere, and at these higher altitudes the particle densities are too low for efficient production of bremsstrahlung. We segmented the differential intensity data into downward and upward electrons by loss cone intervals (defined for each pole)¹⁹. We found that the spectral shape of the precipitating electrons was insensitive to the selection of a loss cone range, even between pitch angles $\theta = 12^\circ$ and $\theta = 90^\circ$. Pitch angles are locally defined with respect to the magnetic field orientation measured by the *Juno*/MAG instrument. The lower limit of the pitch angle range, corresponding to the integral range of differential electron flux, is set to the FOV of a single JEDI detector. Note that the MAG data are well characterized by the JRM09 model which represents the global magnetic field geometry²⁰, while the perturbation by the Birkeland current is negligible ($< 1\%$)¹⁷. Thus, the pitch angle data obtained by JADE, JEDI and MAG instruments accurately reflect the electron current's directions above the auroral regions. In the end, we adopted the values found in Allegrini¹⁹, $\theta < 44^\circ$ for the northern aurora

and $\theta < 37^\circ$ for the southern aurora, for constructing the flux data for precipitating electrons. The electron flux normalization varies linearly with the loss cone angle range. JADE is composed of three separate instruments which, when combined, offer complete pitch angle coverage. However, one of these instruments (*JADE 300*) malfunctioned in flight and had been switched off, resulting in incomplete pitch angle coverage. To rectify this effect, we excluded electron data for the time intervals when the full loss cone coverage was not obtained by JADE.

We produced spectra of the precipitating electrons for each pole and JADE/JEDI instrument by averaging over the period for which *Juno*'s magnetic footprint overlapped the auroral oval and across all look directions within the defined loss cones. Merging the observations of these two instruments into a single electron spectrum required some modification in the 30–100 keV band where the two instruments overlap. Since JADE has higher energy resolution than JEDI in this energy range, we rebinned JADE spectra to match up with the JEDI energy bins. This re-binned spectra was then averaged with the JEDI data for fitting purposes. The resulting electron spectra, constructed from the JADE and JEDI data, spanned from 0.1 keV to 1 MeV with only a small discrepancy between the two instruments. Figure 3 shows the precipitating electron spectra of the northern and southern aurorae, taken by JADE and JEDI instruments during PJ 6, 7 and 12. We fit a power-law model ($I(E_e) \propto E_e^{-\alpha_e}$) to characterize JADE, JEDI and joint spectra (Extended Data Table 2). In several instances, a power-law model did not yield a good fit to the joint JADE + JEDI spectra (e.g., the north pole orbit in PJ 7). Otherwise, the JADE, JEDI and joint spectra are well characterized by a power-law model yielding the best-fit spectral index from $\alpha_e = 0.7$ to 1.9 (Extended Data Table 2). The power-law form of the electron spectra of Figure 3, with

the possible exception of north pole PJ 7, is evidence of electrons accelerated by stochastic or broadband acceleration¹⁰. The north pole PJ 7 spectrum shows a positive slope just above ~ 100 keV. But the spectral slope $\alpha_e \sim -0.65$ to -0.95 is shallower than the $\alpha_e \lesssim -1$ characteristic of coherent acceleration by magnetically-aligned electric fields. Consequently we calculated the average electron spectral index, including all six *Juno* orbits ($\bar{\alpha}_e = 1.30$). For the reason noted just above, the average spectral index is unchanged by the exclusion of north pole PJ 7 data. Note that we did not weight the spectral index by the measured electron fluxes since the *Juno*'s orbit altitude varied between the observations (thus likely leading to different electron fluxes). Hereafter, we assumed that the precipitating electron spectra follow a power-law model of $\alpha_e = 1.3$.

Spatial and temporal variability of the JADE/JEDI electron flux. Since the cumulative observation time of the *Juno* orbits (7 ksec) is a small fraction of the *NuSTAR* exposure, the spatial and temporal variability of the precipitating electron flux may affect the flux normalization of our model X-ray spectra. In order to investigate the electron flux variability, we extracted JADE/JEDI electron data from a 2-minute time interval of all available *Juno* orbits (PJs 1–24 excluding PJ2) around their perijove points. The 2-minute interval was selected to ensure that *Juno* would complete two rotations on either side of the perijove point. The total electron flux above 3 keV, after averaging over all time intervals and look directions, was calculated for each orbit. We found a factor of 2.1 variability between different *Juno* orbits, representing the temporal variability over weeks to months. In addition, as shown in Extended Data Fig. 1, the electron count rate significantly changed in each *Juno*'s orbit. Thus, the selection of a loss cone and X-ray emission area (through the pitch angle range and time interval from which electron data are extracted), both of

which cannot be completely determined from the current in-site and X-ray observations, can result in additional flux uncertainties. These effects likely caused the electron flux variability by a factor of 1.9–3.0 and 1.2–1.4 in the northern and southern pole, respectively, between PJ 6, 7 and 12 (Extended Data Table 2). Overall, we estimated the electron (and thus X-ray) flux errors up to a factor of $\sim 2 - 3$.

Simulation of electron bremsstrahlung spectra in the Jovian atmosphere. Given the complexity of electron propagation and bremsstrahlung X-ray emission in the Jovian atmosphere, we utilized the widely-used particle propagation simulator GEANT4^{22,39}. Our Monte-Carlo simulation approach, by taking into account the electron energy distribution measured in-situ, the most updated particle/atomic database and a more realistic Jovian atmosphere profile, supercedes the original calculation of Singhal in 1992⁸ and is similar to the approach utilized for Earth X-ray modeling by Woodger (2015)²⁵. Our simulation employs the Electromagnetic Penelope Physics List, which agrees most accurately with experimental bremsstrahlung results below 3 MeV⁴⁰. In our simulation, we modeled a stratified Jovian atmosphere based on the density/temperature profiles of the polar regions obtained by Atreya^{23,24} and Livengood⁴¹. The model atmosphere is a spherical shell with the Jovian radius and a thickness of 80,000 km which corresponds to *Juno*'s perijove altitude, divided into four distinct regions (see below) and composed of 80 total layers of molecular/atomic hydrogen, helium atoms, and methane. The fraction of other species is negligible. Each layer's thickness was set such that none of the parameters (temperature, density, or pressure) varies by more than a factor of 2 across the layer. We found this configuration optimal for achieving the most robust results within reasonable CPU time, after testing various cases. Since

initial simulations demonstrated that X-rays were exclusively produced below 700 km of altitude, we decreased the thickness of these layers to 10 km and achieved a smooth X-ray emissivity curve as a function of altitude (Extended Data Fig. 2). The finer altitude depths removed numerical glitches which are artificially produced as a result of the typical bremsstrahlung interaction length being shorter than the grid size.

The model atmosphere consists of four regions, each of which has been characterized by attributes in its profile. (1) Region 1: The lowest of these regions consists of 43 layers over $h = 430$ km measured from the Jovian surface at $1 R_J$. It is characterized by a narrow temperature range of 150–200 K but a steep density variation. These layers are composed entirely of molecular hydrogen, helium, and methane mixed at the average fractional ratios for Jupiter’s atmosphere²³. (2) Region 2: Above this is a region at $h = 430–1400$ km, characterized by the rapid change in temperature (a gradient of ~ 1 K/km) connecting the low temperature region below it to the high temperature (~ 1200 K) region above it²⁴. Within this region, the chemical composition varies dramatically, largely due to the steep temperature gradient: methane does not exist in significant quantities in this region and helium becomes increasingly sparse until the atmosphere is dominated entirely by molecular hydrogen. Then, atomic hydrogen begins to become more prominent as hydrogen molecules become dissociated at higher temperatures. (3) Region 3: The top atmospheric region at $h = 1400–5000$ km is characterized by an exponential density profile. It is assumed that this region has a constant temperature of 1,200 K, but our simulation is insensitive to this specific temperature. (4) Region 4: The *Juno* observations during PJ 6, 7, and 12 occurred at an average height of 83,800 km, far above the atmospheric regions mentioned above. To fill in the gap, we

introduced a single homogeneous layer of 75,000 km height and composed of atomic hydrogen. In this region we assumed a constant density of 50 cm^{-3} , similar to the ion density value measured by *Juno*⁴². Given the small total hydrogen column density ($N_{\text{H}} < 10^{13} \text{ cm}^{-2}$), this above-the-atmosphere region has a negligible impact on electron deceleration and X-ray emission/absorption. As mentioned above, the average JADE and JEDI electron spectra are well characterized by a single power-law model with $\alpha_e \approx 1.3$ up to $\sim 1 \text{ MeV}$. In each simulation, we randomly injected 100 million primary electrons between 3 keV and 1 MeV from a power-law distribution with $\alpha_e = 1.3$. While a majority of the primary electrons are eventually absorbed in the atmosphere, the number of injected electrons is sufficient to characterize X-ray spectra and compare well with the *NuSTAR* and *XMM-Newton* spectra. We collected X-ray photons escaping from the spherical atmosphere at its top. Most of the precipitating electrons emit bremsstrahlung X-rays at the upper atmospheric depths corresponding to $N_{\text{H}} \lesssim 10^{22} \text{ cm}^{-2}$ (mostly in Region 1 and 2). As shown in Extended Data Fig. 2, X-ray emissivity drops sharply below $\sim 200 \text{ [km]}$ in Region 1 where the neutral hydrogen column density dramatically increases ($N_{\text{H}} \gtrsim 10^{25} \text{ cm}^{-2}$). On the other hand, X-rays are scarce above $\sim 600 \text{ [km]}$ since the hydrogen density is not high enough to emit bremsstrahlung X-rays. Note that X-ray photons should escape from the auroral regions at $80\text{--}90^\circ$ degrees with respect to the pole (in the direction of Earth) in order to be observed by X-ray telescopes⁴³. However, X-ray bremsstrahlung photons above $E \sim 3 \text{ keV}$ do not suffer from limb darkening since the photo-absorption and Compton scattering are insignificant at the atmospheric depths where they are emitted.

In order to compute the total X-ray luminosity emitted from both auroral regions, we mul-

multiplied the integrated electron flux obtained by JADE/JEDI, by an electron-to-X-ray conversion factor, and the projection of the emitting area of the two auroral regions (A) onto Juno's orbital altitude. For simplicity, we adopted $A = 1 \times 10^{20} \text{ cm}^2$, corresponding to the area of the UV ovals which overlap with the X-ray continuum emission above $E \sim 2 \text{ keV}$ ⁴⁴ assuming that the electron flux is spatially uniform over the auroral regions. Since *Juno*'s orbits during the perijoves covered only a portion of the magnetic field lines above the aurorae, this assumption may lead to errors in the predicted X-ray flux if the electron current is not spatially uniform over the oval region, since this causes electron flux variability as discussed in the previous section. From the GEANT4 simulation, we determined the ratio of the number of X-rays to the number of primary electrons in the 3–20 keV band. This ratio is about 5.8×10^{-4} . Since our simulation results showed that the bremsstrahlung X-ray emission is nearly isotropic, we computed X-ray flux by dividing the X-ray luminosity by $4\pi d^2$ where d is the average distance of Jupiter ($7.24 \times 10^{13} \text{ cm}$; weighed by exposure time of each *NuSTAR* observation) during the *NuSTAR* observations.

If we adopt the average electron spectra from PJ 6, 7 and 12, the estimated 3–20 keV flux of $9.1 \times 10^{-7} \text{ photons/cm}^2/\text{s}$ is a factor of 3.6 smaller than the measured X-ray flux of $3.3_{-0.8}^{+0.2} \times 10^{-6} \text{ photons/cm}^2/\text{s}$, while the observed X-ray spectral shape obtained from *NuSTAR*, *XMM-Newton* and *Ulysses* data are well reproduced (Figure 2). The flux normalization discrepancy is likely due to the spatial/temporal electron flux variation over the auroral regions (as discussed in the previous section) as well as uncertainties associated with the selection of a loss cone and X-ray emitting area. We found that the electron flux varied between different *Juno* perijoves by a factor of 2.1 (1- σ standard deviation between all available perijoves) to 3 (the maximum flux

variation between PJ 6, 7 and 12). For instance, if we take the highest electron fluxes measured in each pole during PJ 6, 7 and 12, the estimated 3–20 keV flux of 2.4×10^{-6} photons/cm²/s is consistent with the measured X-ray flux (i.e. a factor of 1.4 lower but within the statistical errors). In addition, any uncertainty associated with the loss cone and X-ray emitting area should affect the predicted X-ray flux linearly. We also took into account the possibility that multi-MeV energy electrons populate the Jovian magnetosphere beyond the JADE/JEDI energy band (> 1 MeV) as suggested by recent *Juno* observations²⁷. When we extended the best-fit power-law model up to $E_{\text{max}} = 2$ and 5 MeV, we found that the flux normalization discrepancy decreases to a factor of 2.2 and 0.96, respectively. This is due to the contribution of additional X-ray emission from higher energy electrons that terminate deeper in the atmosphere. However, we found that simulated X-ray spectra with $E_{\text{max}} \gtrsim 1$ MeV are harder than the observed X-ray spectra (e.g., $\chi^2_{\nu} = 1.25$ with 35 dof for $E_{\text{max}} = 2$ MeV). Furthermore, our X-ray modeling with GEANT4, consistent with the work of previous authors^{4,25}, ignores magnetic mirroring. This effect should produce higher downward electron fluxes above the atmosphere at $\sim 1R_J$ (thus leading to higher X-ray fluxes) compared to the fluxes measured at higher altitudes $\sim 2R_J$ corresponding to the perijoves. This would systematically increase our modeled X-ray fluxes, bringing them more into agreement with the observations. Given the electron flux variability, statistical errors related to the X-ray flux, and these other systematics, we consider that the observed and predicted X-rays fluxes are consistent with each other.

Simulated X-ray spectra are plotted in Figure 4, as well as in Figure 2 along with the *NuSTAR* and *XMM-Newton* spectra. The predicted and observed X-ray spectra are similar to each

other, exhibiting a hard spectral index ($\Gamma \approx 0.6$) then spectral softening (which is consistent with the *Ulysses* X-ray flux upper limits in the 27–48 keV), after matching the flux normalization between the spectra. We found that this characteristic X-ray spectral shape is robust by inputting other electron spectral indices (from $\alpha_e \sim 0.8$ to 1.7 measured by *Juno*) than the average value ($\alpha_e = 1.3$) in the GEANT4 simulation. We note that deceleration of electrons in the upper atmosphere is required to reproduce the flat X-ray spectra with $\Gamma \approx 0.6$ (3–20 keV); the precise spectral shape results largely from the energy-dependence of the electron stopping power (dE_e/dx) increasing at lower electron energy, $E_e \lesssim 1$ MeV. We also found that the Jovian atmosphere density profile reproduces the observed X-ray spectral shape well; atmosphere layers with higher column densities yielded too soft model spectra, compared to the measured X-ray photon index in the 3–20 keV band, by overproducing low-energy X-rays. Thus, we emphasize that the consistency between the observed and predicted X-ray spectra is a natural consequence of propagating the *Juno* electron data taken during the perijoves into the realistic Jovian atmosphere model – there is no parameter fitting besides the X-ray flux normalization. Our analysis and simulation, based on the simultaneous *NuSTAR*, *XMM-Newton* and *Juno* observations, establishes that the X-ray continuum emission from the Jovian aurorae originates from precipitating non-thermal electrons in the upper atmosphere.

Data availability The *NuSTAR* and *XMM-Newton* data are archived at NASA’s HEASARC website. The *JEDI*, *JADE*, and *MAG* data are available at the Planetary Data System. The magnetic footprint of *JUNO* is available through the LASP MOP group’s website.

Code availability *NuSTAR* and *XMM-Newton* data are analyzed by HEASOFT and SAS analysis soft-

ware, respectively. Geant4 simulation tool is publicly available at <https://geant4.web.cern.ch>. The simulation and data reduction code is available upon request.

Correspondence Correspondence and requests for materials should be addressed to Kaya Mori (email: kaya@astro.columbia.edu).

Acknowledgements We thank Dr. Rob Wilson for his help in analyzing JADE data. We further thank the MOP group of LASP for their work on Juno's trajectory and magnetic footprint. We acknowledge Dr. Daniel Wik for his help in analyzing *NuSTAR* background data. We are grateful for the referees for making useful comments. Support for this work by K.M was provided by NASA through *NuSTAR* Cycle 3 Guest Observer Program grant NNH16ZDA001N. C. M. J.'s work at DIAS was supported by the Science Foundation Ireland Grant 18/FRL/6199.

Author contributions K.M., C.H., G.B. and S.M. wrote the manuscript and made large contributions to data analysis and interpretation. G.B. performed JADE/JEDI data analysis and GEANT4 simulations. S.M. and B.J.H. analyzed *NuSTAR* data. B.G. contributed to *NuSTAR* data analysis and interpretation. A.G. and W.D. were involved with *XMM-Newton* data analysis. J.C. and M.N. conducted a feasibility study of *NuSTAR* observations of Jupiter. G.B.-R., C.J. and L.R. interpreted the analysis results and provided insights to the Jovian aurora physics. All authors contributed to discussing the results and commenting on the manuscript.

Competing interests The authors declare that they have no competing financial interests.

Data availability The *NuSTAR* and *XMM-Newton* data are archived at NASA's HEASARC website. The JEDI, JADE, and MAG data are available at the Planetary Data System. The magnetic footprint of JUNO is

available through the LASP MOP group's website.

Code availability NuSTAR and XMM-Newton data are analyzed by HEASOFT and SAS analysis software, respectively. Geant4 simulation tool is publicly available at <https://geant4.web.cern.ch>. The simulation and data reduction code is available upon request.

Correspondence Correspondence and requests for materials should be addressed to Kaya Mori (email: kaya@astro.columbia.edu).

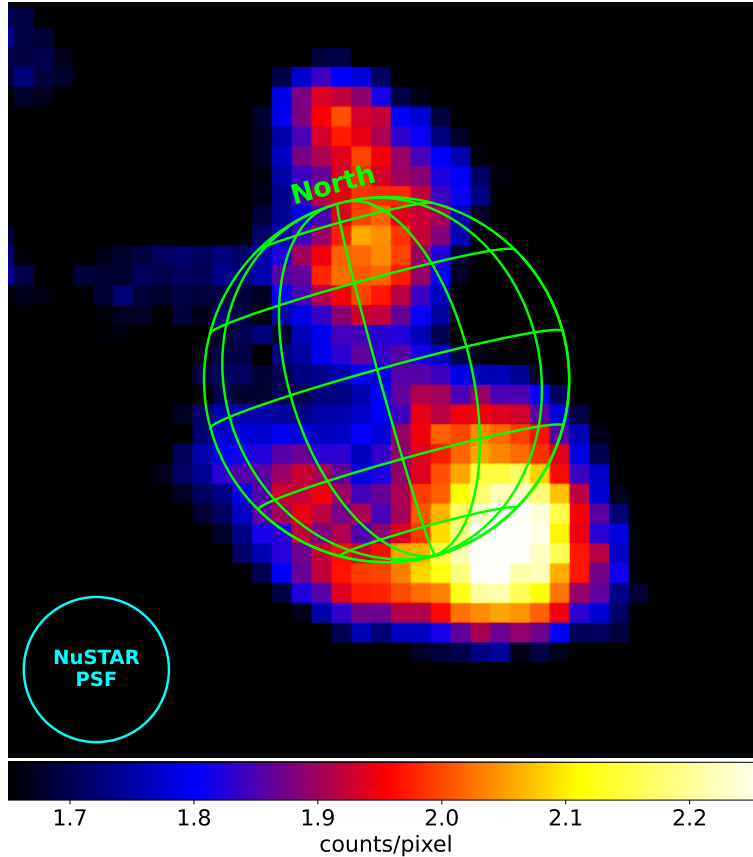


Figure 1: *NuSTAR* 8–20 keV image of Jupiter overlaid on a graticule which shows the geometry of the planet during PJ12 ($r = 42.6''$). The north pole is indicated by "North" in the graticule. The angular size of Jupiter varies between $r = 37''$ and $45''$ during the five *NuSTAR* observations. We combined FPMA and FPMB images after smoothing by a gaussian kernel with $\sigma = 6$ pixels ($15''$). The *NuSTAR* PSF (FWHM = $18''$ shown in the lower left corner), is comparable to the size of each auroral region, thus it is not feasible to correlate the hard X-ray emission with the UV oval or soft X-ray polar region. The northern and southern auroral regions, defined by a $r = 25''$ circle around each pole, yielded 114 and 229 counts, respectively, in the 8–20 keV band.

Extended Data Table 1: *NuSTAR* observations of Jupiter

Observation date	Distance [AU]	Exposure [ksec]	Net ^a counts	Detection σ	Juno orbit	Simultaneous observations
01/30/2015	4.4	102.6	105	3.3	—	—
05/16/2017	4.7	134.5	132	3.2	PJ6	<i>Chandra</i>
06/18/2017	5.1	101.5	130	3.4	AJ7	<i>Chandra, XMM, HST</i>
07/10/2017	5.4	134.2	163	4.2	PJ7	<i>Chandra, XMM, HST</i>
04/01/2018	4.6	126.3	197	5.0	PJ12	<i>Chandra</i>

^a Net count rates in the 3–20 keV band. Both FPMA and FPMB counts are combined. Source and background counts were extracted from a $r = 45''$ circle and a $r = 60–75''$ annular region around the Jovian center, respectively.

Extended Data Table 2: *Juno* orbits coincident with *NuSTAR* observations and electron spectral parameters

<i>Juno</i> Orbit	Orbit Date	Pole	Time	R_J	α_e	Electron flux [electrons/cm ² /s]
PJ 6	05/19/2017	North	00:57:11	7.03	$1.26 \pm .05$	1.16×10^5
		South	06:49:00	1.87	$1.41 \pm .61$	3.50×10^5
PJ 7	07/11/2017	North	01:19:00	1.59	$1.89 \pm .14$	2.79×10^6
		South	02:30:00	1.57	1.01 ± 0.03	5.78×10^5
PJ 12	04/01/2018	North	07:32:00	3.77	1.54 ± 0.08	4.82×10^4
		South	10:42:30	2.12	0.67 ± 0.01	5.36×10^5

Note: α_e is the best-fit spectral index of JADE + JEDI electron spectra in each *Juno* passage. The

last column lists the downward electron flux in the 3keV – 1 MeV band.

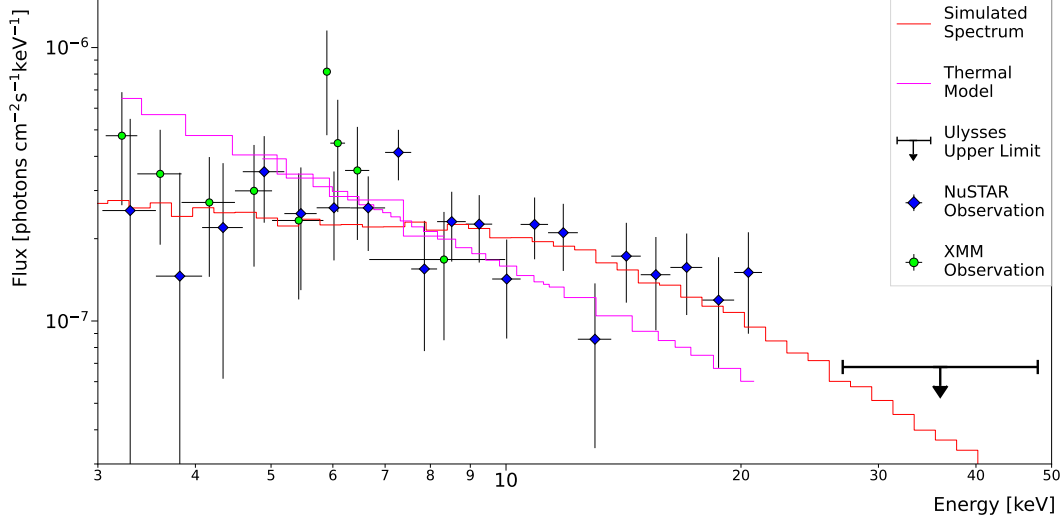


Figure 2: *XMM-Newton-EPIC* and *NuSTAR* flux spectra of Jupiter (green and blue, respectively) with simulated spectrum (red) and best-fit thermal bremsstrahlung model ($kT = 200$ keV; magenta). Both *NuSTAR* and *XMM-Newton* spectra are binned to a minimum detection significance of $\sigma \geq 2$. The *NuSTAR* spectra are further rebinned in the plot for better visualization. X- and Y-errors represent the energy bin sizes and $1-\sigma$ statistical errors, respectively. The 27–48 keV flux upper limits ($3-\sigma$) obtained by the in-situ *Ulysses* measurements¹¹ are indicated by an arrow. The fit with the simulated spectrum ($\chi^2_\nu = 1.1$ for 35 dof) is better than that of the thermal bremsstrahlung model ($\chi^2_\nu = 1.5$ for 34 dof). The Akaike information criterion test yields $\Delta\text{AIC} = 14.9$, indicating that the simulation model is preferred over the thermal bremsstrahlung model by a relative likelihood of 3×10^6 . The simulated spectrum's flux normalization has been multiplied by a factor of 3.6 in order to match the X-ray flux observed by *XMM-Newton* and *NuSTAR*.

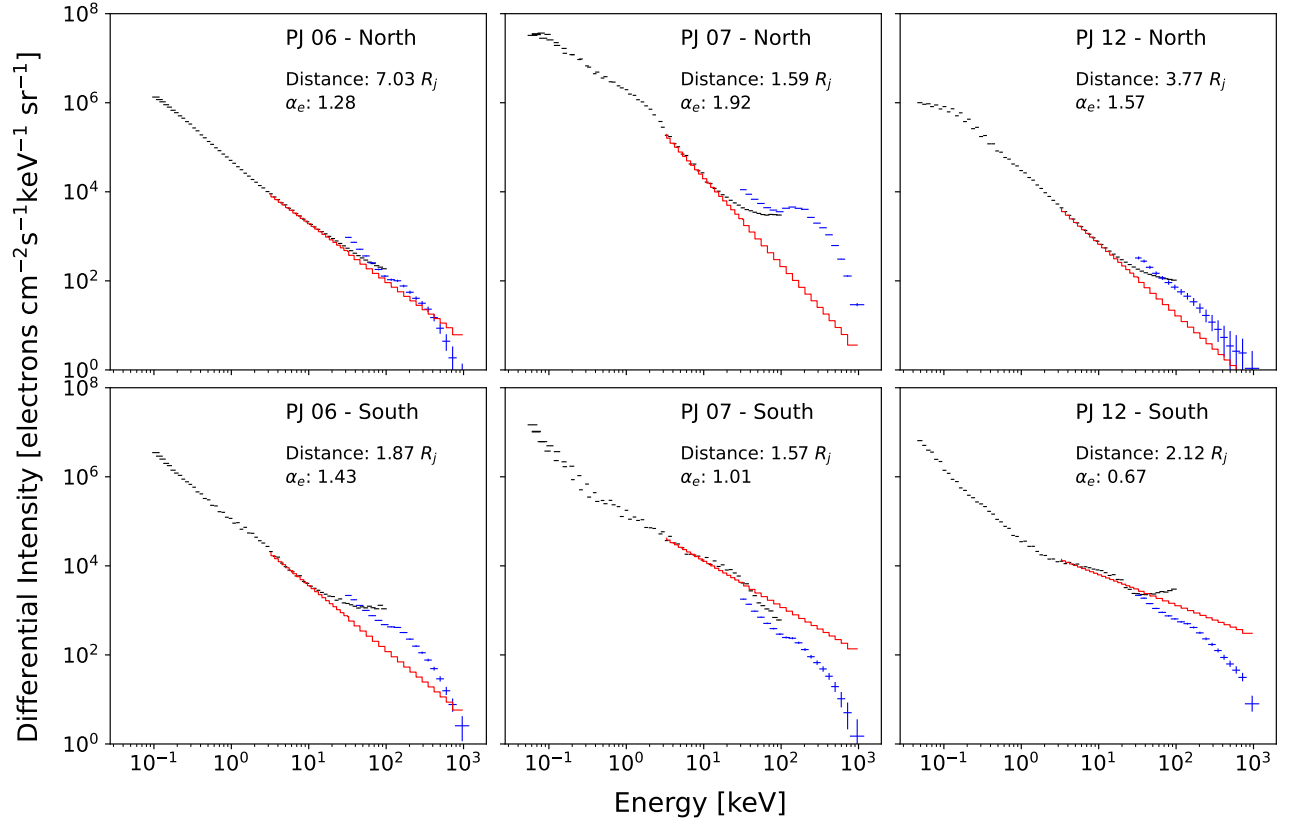


Figure 3: JADE (black) and JEDI (blue) energy spectra of precipitating electrons in the north (top panels) and south (bottom panels) for PJ 6 (left), 7 (middle), and 12 (right). The power-law models fit from 3 keV to 1 MeV, corresponding to the energy range of electrons that produce 3–20 keV bremsstrahlung X-rays in the Jovian atmosphere, are overlaid in red. The best-fit power-law index (α_e) and the distance of *Juno* from the Jovian center (in unit of the Jovian radius R_J) are listed in each panel. The corresponding *Juno* observations and more details are listed in Extended Data Table 2.

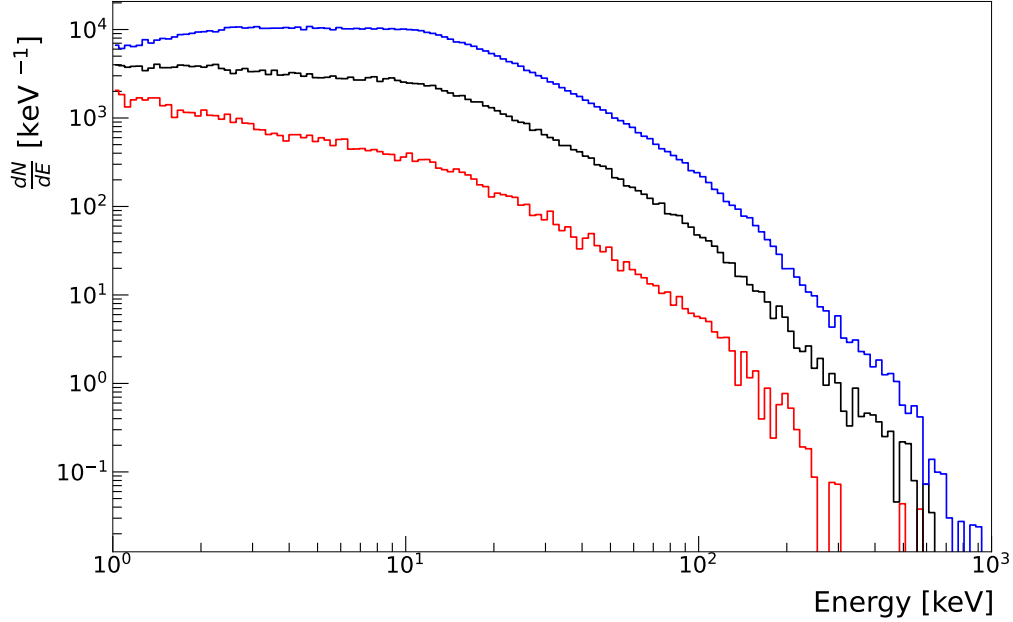
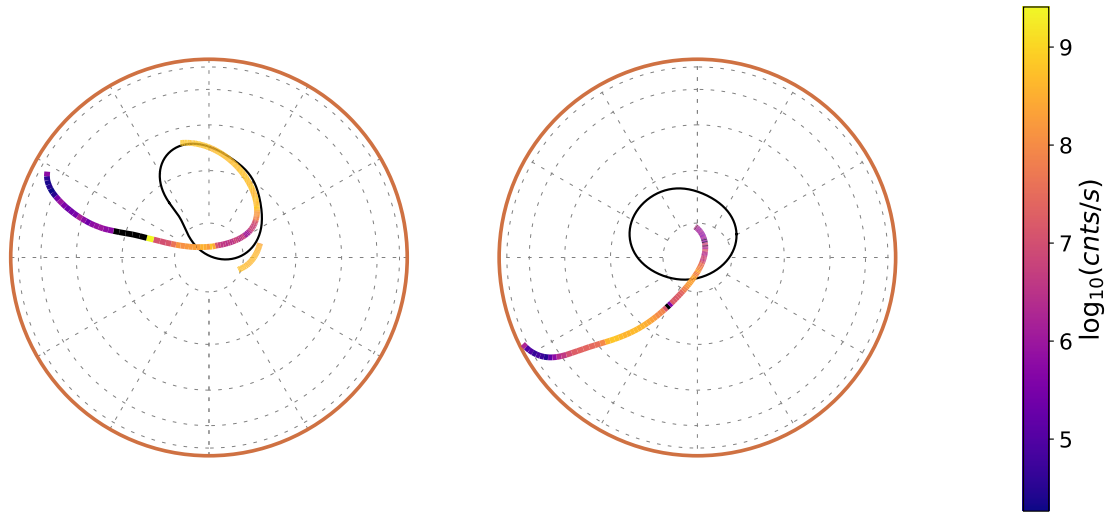
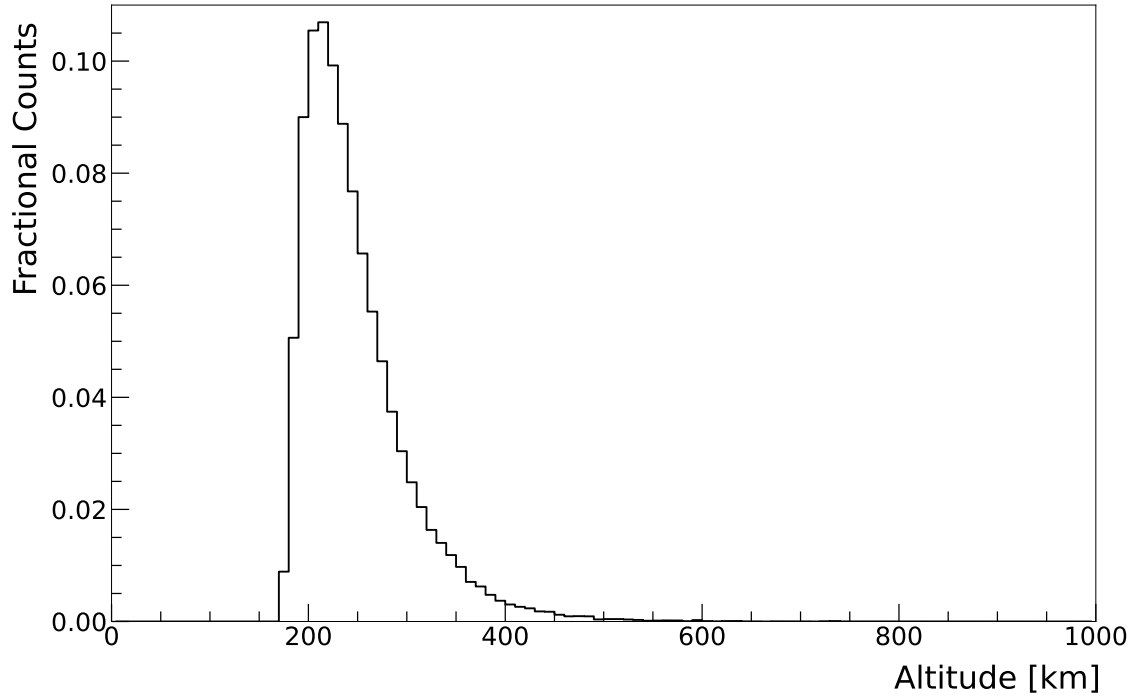


Figure 4: Simulated spectra of X-ray photons escaping from the model atmosphere for three different electron spectra. The spectra are plotted in counts per energy bin vs photon energy [keV]. We input the mean electron spectrum (black) from the *Juno* observations listed in Extended Data Table 2 into the GEANT4 simulator, as well as the hardest (blue) and softest (red) spectra observed by *Juno*. The simulated X-ray spectra are characterized by a flat power-law component ($\Gamma \sim 0.03\text{--}0.4$) up to $E \sim 10$ keV, followed by a softer power-law component ($\Gamma \sim 1$). Fitting a single power-law model to the simulated X-ray spectra in the 3–20 keV band, where we obtained *XMM-Newton* and *NuSTAR* spectra, yields $\Gamma = 0.2\text{--}0.7$, which is consistent with the observed X-ray photon index ($\Gamma = 0.60 \pm 0.22$).



Extended Data Fig. 1: Magnetic footprint of Juno as viewed from above the north (left) and south (right) poles in PJ12. Black ovals represent the UV ovals³⁸. The color bar indicates the net electron counts obtained by JADE across all energy channels and look directions (in logarithmic scale). A region in the *Juno* orbit (indicated by black), where background counts exceeded signal counts, was removed from our analysis. We obtained coordinates for the auroral ovals and JRM09 magnetic footprint²⁰ from the MOP LASP website. All coordinates are SYS III.



Extended Data Fig. 2: Counts of escaping X-rays as a function of the altitude [km] (which is measured from $1 R_j$). The counts drop sharply below $h \sim 200$ [km] as X-rays are heavily absorbed. The altitude range shown in the plot cover Region 1 and 2 described in the Method. Note that most of escaping X-rays are from Region 1 ($h < 430$ km).

1. Li, Z. *et al.* Investigation of EMIC wave scattering as the cause for the BARREL 17 January 2013 relativistic electron precipitation event: A quantitative comparison of simulation with observations. *Geophys. Res. Lett.* **41**, 8722–8729 (2014).
2. Lorentzen, K. R. *et al.* Precipitation of relativistic electrons by interaction with electromagnetic ion cyclotron waves. *J. Geophys. Res.* **105**, 5381–5390 (2000).
3. Millan, R. M., Lin, R. P., Smith, D. M., Lorentzen, K. R. & McCarthy, M. P. X-ray observations of MeV electron precipitation with a balloon-borne germanium spectrometer. *Geophys. Res. Lett.* **29**, 2194 (2002).
4. Foat, J. E. *et al.* First detection of a terrestrial MeV X-ray burst. *Geophys. Res. Lett.* **25**, 4109–4112 (1998).
5. Branduardi-Raymont, G. *et al.* A study of Jupiter’s aurorae with XMM-Newton. *Astron. Astrophys.* **463**, 761–774 (2007). astro-ph/0611562.
6. Barbosa, D. D. Bremsstrahlung X rays from Jovian auroral electrons. *J. Geophys. Res.* **95**, 14969–14976 (1990).
7. Waite, J., J. H., Boice, D. C., Hurley, K. C., Stern, S. A. & Sommer, M. Jovian Bremsstrahlung X rays: A Ulysses prediction. *Geophys. Res. Lett.* **19**, 83–86 (1992).
8. Singhal, R. P., Chakravarty, S. C., Bhardwaj, A. & Prasad, B. Energetic electron precipitation in Jupiter’s upper atmosphere. *J. Geophys. Res.* **97**, 18245–18256 (1992).

9. Wibisono, A. D. *et al.* Temporal and Spectral Studies by XMM-Newton of Jupiter's X-ray Auroras During a Compression Event. *J. Geophys. Res. Space Phys.* **125**, e27676 (2020).
10. Mauk, B. H. *et al.* Discrete and broadband electron acceleration in Jupiter's powerful aurora. *Nature* **549**, 66–69 (2017).
11. Hurley, K., Sommer, M. & Waite, J. H. Upper limits to Jovian hard X radiation from the Ulysses gamma ray burst experiment. *J. Geophys. Res.* **98**, 21217–21220 (1993).
12. Harrison, F. A. *et al.* The Nuclear Spectroscopic Telescope Array (NuSTAR) High-energy X-Ray Mission. *Astrophys. J.* **770**, 103 (2013). 1301.7307.
13. Dunn, W. R. *et al.* The impact of an ICME on the Jovian X-ray aurora. *J. Geophys. Res. Space Phys.* **121**, 2274–2307 (2016).
14. Jackman, C. M. *et al.* Assessing Quasi-Periodicities in Jovian X-Ray Emissions: Techniques and Heritage Survey. *J. Geophys. Res. Space Phys.* **123**, 9204–9221 (2018).
15. Cowley, S. W. H. & Bunce, E. J. Origin of the main auroral oval in Jupiter's coupled magnetosphere-ionosphere system. *Planet. Space Sci.* **49**, 1067–1088 (2001).
16. Dunn, W. R. *et al.* The independent pulsations of Jupiter's northern and southern X-ray auro-
ras. *Nat. Astron.* **1**, 758–764 (2017).
17. Kotsiaros, S. *et al.* Birkeland currents in Jupiter's magnetosphere observed by the polar-orbiting Juno spacecraft. *Nat. Astron.* **3**, 904–909 (2019).

18. Clark, G. *et al.* Energetic particle signatures of magnetic field-aligned potentials over Jupiter's polar regions. *Geophys. Res. Lett.* **44**, 8703–8711 (2017).
19. Allegrini, F. *et al.* Electron beams and loss cones in the auroral regions of Jupiter. *Geophys. Res. Lett.* **44**, 7131–7139.
20. Connerney, J. E. P. *et al.* A New Model of Jupiter's Magnetic Field From Juno's First Nine Orbits. *Geophys. Res. Lett.* **45**, 2590–2596 (2018).
21. Clark, G. *et al.* Precipitating Electron Energy Flux and Characteristic Energies in Jupiter's Main Auroral Region as Measured by Juno/JEDI. *J. Geophys. Res. Space Phys.* **123**, 7554–7567 (2018).
22. Agostinelli, S. *et al.* GEANT4—a simulation toolkit. *Nucl. Instrum. Methods Phys. Res. Sect. A Accel. Spectrom. Detect. Assoc. Equip.* **506**, 250–303 (2003).
23. Atreya, S., Mahaffy, P., Niemann, H., Wong, M. & Owen, T. Composition and origin of the atmosphere of Jupiter — an update, and implications for the extrasolar giant planets. *Planet. Space Sci.* **51**, 105 – 112 (2003).
24. Atreya, S. K., Donahue, T. M. & Festou, M. Jupiter - Structure and composition of the upper atmosphere. *Astrophys. J. Lett.* **247**, L43–L47 (1981).
25. Woodger, L. A. *et al.* A summary of the BARREL campaigns: Technique for studying electron precipitation. *J. Geophys. Res. Space Phys.* **120**, 4922–4935 (2015).
26. Saur, J. *et al.* Anti-planetward auroral electron beams at Saturn. *Nature* **439**, 699–702 (2006).

27. Paranicas, C. *et al.* Intervals of Intense Energetic Electron Beams Over Jupiter's Poles. *J. Geophys. Res. Space Phys.* **123**, 1989–1999 (2018).
28. Abazajian, K. N. *et al.* The Seventh Data Release of the Sloan Digital Sky Survey. *Astrophys. J. Suppl. Ser.* **182**, 543–558 (2009). 0812.0649.
29. Wik, D. R. *et al.* NuSTAR Observations of the Bullet Cluster: Constraints on Inverse Compton Emission. *Astrophys. J.* **792**, 48 (2014). 1403.2722.
30. Scargle, J. D., Norris, J. P., Jackson, B. & Chiang, J. Studies in Astronomical Time Series Analysis. VI. Bayesian Block Representations. *Astrophys. J.* **764**, 167 (2013). 1207.5578.
31. McComas, D. *et al.* The Jovian Auroral Distributions Experiment (JADE) on the Juno Mission to Jupiter. *Space Sci. Rev.* **213**, 547–643 (2017).
32. Mauk, B. *et al.* The Jupiter Energetic Particle Detector Instrument (JEDI) Investigation for the Juno Mission. *Space Sci. Rev.* **98**, 98– (2013).
33. Allegrini, F., Wilson, R., Ebert, R. & Loeffler, C. JUNO JADE Calibrated Science Data (NASA Planetary Data System, 2019). URL https://pds-ppi.igpp.ucla.edu/data/JNO-J_SW-JAD-3-CALIBRATED-V1.0/.
34. JUNO JEDI Jupiter Standard Calibrated Products (NASA Planetary Data System, 2020). URL <https://pds-ppi.igpp.ucla.edu/data/JNO-J-JED-3-CDR-V1.0/> (2020).

35. Connerney, J. JUNO Magnetometer Jupiter Archive (NASA Planetary Data System, 2020).
URL <https://pds-ppi.igpp.ucla.edu/data/JNO-J-3-FGM-CAL-V1.0/>
(2020).
36. Acton, C., Bachman, N., Semenov, B. & Wright, E. A look towards the future in the handling of space science mission geometry. *Planet. Space Sci.* **150**, 9 – 12 (2018).
37. Allegrini, F. *et al.* Energy Flux and Characteristic Energy of Electrons Over Jupiter's Main Auroral Emission. *J. Geophys. Res. Space Phys.* **125**, e2019JA027693.
38. Bonfond, B. *et al.* Auroral evidence of Io's control over the magnetosphere of Jupiter. *Geophys. Res. Lett.* **39**.
39. Allison, J. *et al.* Geant4 developments and applications. *IEEE Trans. Nucl. Sci.* **53**, 270–278 (2006).
40. Pandola, L., Andenna, C. & Caccia, B. Validation of the GEANT4 simulation of bremsstrahlung from thick targets below 3 MeV. *Nucl Instrum Methods Phys Res B* **350**, 41 – 48 (2015).
41. Livengood, T. A., Strobel, D. F. & Moos, H. W. Long-term study of longitudinal dependence in primary particle precipitation in the north Jovian aurora. *J. Geophys. Res. Space Phys.* **95**, 10375–10388.
42. Valek, P. W. *et al.* Jovian High-Latitude Ionospheric Ions: Juno In Situ Observations. *Geophys. Res. Lett.* **46**, 8663–8670.

43. Ozak, N., Schultz, D. R., Cravens, T. E., Kharchenko, V. & Hui, Y. W. Auroral X-ray emission at Jupiter: Depth effects. *J. Geophys. Res. Space Phys.* **115**, A11306 (2010).
44. Branduardi-Raymont, G. *et al.* Spectral morphology of the X-ray emission from Jupiter's aurorae. *J. Geophys. Res. Space Phys.* **113**, A02202 (2008).